Articular contact vs. embedding: Effect of simplified boundary conditions on the stress distribution in the distal radius and volar plate implant loading

Laurenz Berger[a], Dieter Pahr[a,b], Alexander Synek[a*]

[a]Institute of Lightweight Design and Structural Biomechanics, TU Wien, Vienna, Austria
[b]Division Biomechanics, Karl Landsteiner University of Health Sciences, Krems, Austria
**Corresponding author:* Alexander Synek; Address: Gumpendorfer Straße 7, E317, TU Wien, 1060 Wien; Phone: +43 1 58801 31730; Email: asynek@ilsb.tuwien.ac.at

Keywords:
Distal radius fracture, radiocarpal joint, volar plate, subchondral bone stress, finite element

Version:
Preprint

Abstract:

Boundary conditions (BCs) are often simplified in experimental and numerical models simulating distal radius fractures and their treatments. The aim of this study was to investigate the effects of simplified BCs at the radiocarpal joint: (1) on the stress distribution in the intact distal radius, and (2) on the loading of a volar locking plate (VLP) used for distal radius fracture treatment. Finite element models of the distal radius with contact between the carpals and the cartilage were created as reference models for an intact bone and a fractured bone with VLP treatment. Four models with simplified BCs were compared to these reference models: One with embedding material instead of carpals, one with carpals tied to the radius; each loaded either uniaxially or with statically equivalent loading to the reference model. Differences in distal bone stress distributions and mechanical parameters of the VLP (fracture gap motion, plate peak stresses, distal screw loads) were generally largest for the uniaxially loaded, embedded model (up to 250% in individual screw loads) and smallest for the model with tied carpals and statically equivalent loads (<25% for all parameters). Differences were greatly reduced if statically equivalent loads were applied, but subchondral stress peaks were absent without carpals. Thus, realistic multiaxial loading seems to be most important when modelling the mechanical behavior of the distal radius and fracture treatments. Carpals should be included at least with tied contact to the radius if subchondral bone stresses or individual screw loads of a VLP are investigated.

1. Introduction

Distal radius fractures (DRFs) are among the most common fractures (Nellans et al., 2012). A frequent type of DRF is the Colles' fracture, for which the fracture location lies just 2-3cm proximal from the radio-carpal joint (RCJ) (Baumbach et al., 2011). If the DRF is unstable, treatment typically involves surgical reduction and internal fixation using a volar locking plate (VLP) (Sander et al., 2020).

In the past, finite element (FE) models have been extensively used to investigate DRF mechanics (Edwards and Troy, 2012; Varga et al., 2009) and mechanical parameters after fracture treatment (Knežević et al., 2017; Yamazaki et al., 2021), such as fracture gap movement (FGM) (Caiti et al., 2019; Liu et al., 2020). Still, boundary conditions (BCs) are often highly simplified in these models, which might limit their clinical relevance. For instance, some models simulated uniaxial compression with load application through embedding materials (Synek et al., 2015; Varga et al., 2009) or simply applied the load directly at the articular surface (Caiti et al., 2019; Liu et al., 2020). Only a few included the carpals with contact conditions or at least tied to the radius cartilage (Edwards and Troy, 2012; Pistoia et al., 2002).

Simplifications of BCs are based on the idea that stress distribution differences will decrease quickly with increasing distance from the point of load application, if statically equivalent loads are applied (Saint-Venant, 1855). However, the stresses of interest in the distal radius are close to the point of load application. It is yet unknown to what extent simplifications of BCs influence the stress distributions in the subchondral and Colles' fracture region of the radius and how this error propagates to VLP loading and FGM. The goal of this study was to systematically investigate the effect of simplified BCs (1) on the stress distribution in the intact distal radius and (2) on the mechanical parameters of a fractured distal radius with VLP treatment. To achieve this goal, FE models with contact interaction at the RCJ are established as reference models (RMs) and compared to models with simplified BCs using embedding material or tied contact interaction.

2. Methods

2.1. Intact Bone Reference Model

A computed tomography (CT) scan (male, 53 years, 1.69m, 79kg) from the medical image repository of the Swiss Institute for Computer Assisted Surgery (https://www.smir.ch) (Swiss Institute for Computer Assisted Surgery, 2020) with a voxel size of 1.27x1.27x0.25mm was rescaled to an isotropic resolution of 0.25x0.25x0.25mm and used to segment cortical and trabecular regions and carpals using 3DSlicer (https://www.slicer.org/) (Kikinis et al., 2014). Geometrical model adaptations were performed using Autodesk Fusion 360 (Autodesk, Inc., San Rafael, CA, USA), and the FE model was created in Abaqus 2020 (Dassault Systèmes, Vélizy-Villacoublay, FRA). The coordinate system was defined following the recommendations of the international society of biomechanics (Wu et al., 2005). The bone was cut to a length of 100mm from the tip of the radial styloid process. The articular cartilage was created as a 1mm layer (Pollock et al., 2013) on the distal end of the radius (Figure 1) and connected to the radius using a tie constraint.

Radius and cartilage were meshed with quadratic tetrahedral elements, while carpals were meshed with shell elements. A mesh convergence analysis resulted in an average element size of 1.5mm (see Appendix). Trabecular and cortical regions were modelled as isotropic homogeneous elastic materials (E=1.4GPa and E=17GPa, respectively with v=0.3) (Synek et al., 2015) and the cartilage as a hyperelastic neo-Hookean material with E=10MPa and v=0.45 (Armstrong et al., 1984). The carpals were modelled as a single rigid body. All degrees of freedom were locked at the proximal end of the radius, and only displacement in longitudinal direction was unconstrained for the carpals (Figure 1). A force of 250N was applied on the carpals through a reference point, based on previous estimations of physiological loading in the RCJ (Christen et al., 2013). Contact interaction was modelled between the carpals and the cartilage using a surface-to-surface discretization method with a finite-sliding formulation. Contact was enforced using the augmented Lagrange multiplier method with a hard pressure-overclosure relationship and frictionless behavior.

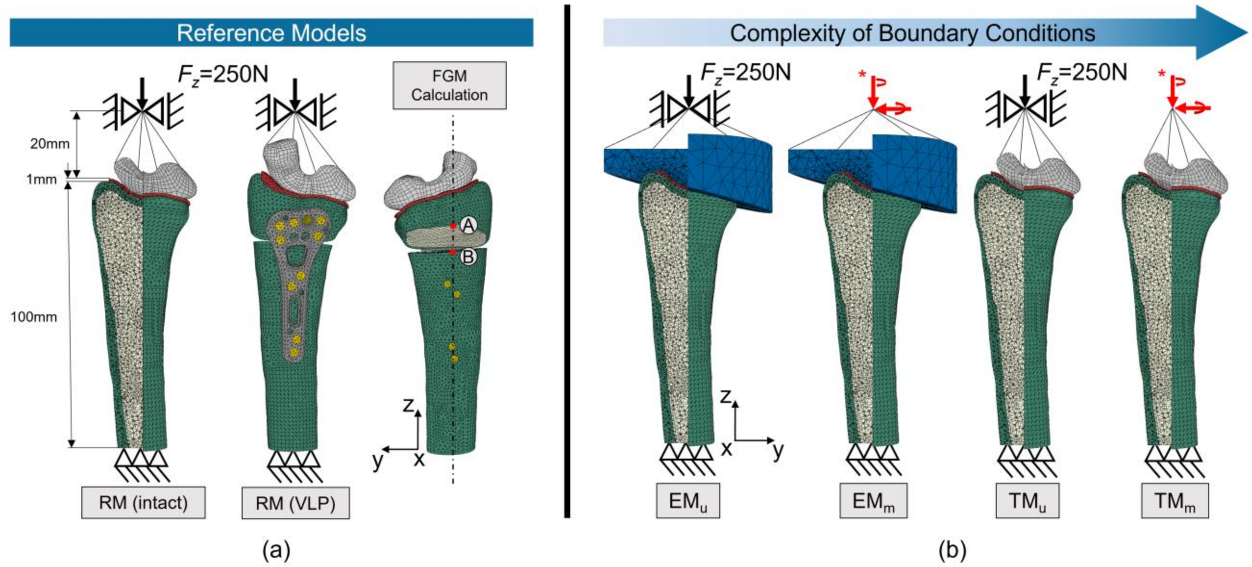

Figure 1: (a) Reference models of both the intact distal radius and the fractured radius with a VLP implant and (b) simplified boundary conditions. Simplified models include the embedded models (EM) and models with tied carpals (TM), each loaded uniaxially (EM_u, TM_u) or multiaxially with load statically equivalent to the reference models (EM_m, TM_m; statically equivalent loads highlighted in red). Points A and B used for fracture gap movement (FGM) calculation.

2.2. Fractured Bone Reference Model

A fractured bone model simulating an extra articular fracture (AO type 23-A3) was established with a 10mm dorsal wedge osteotomy and an angular stable VLP (Aptus Adaptive Distal Radius Plate, Medartis Inc., Basel, Switzerland) with ten screws (Figure 1). Distal screw lengths were chosen as 75% of the measured bicortical length (Baumbach et al., 2015). Screw orientation was standardized using a drill guide block. The VLP was positioned in line with the volar lip of the radius (Schindelar and Ilyas, 2021). All meshing parameters were identical to the intact radius. VLP and screws were modelled as titanium with E=105GPa and v=0.3 (Synek et al., 2021). BCs were applied identically to the RM of the intact bone.

2.3. Simplified Boundary Conditions

Models with simplified BCs involved one model loaded using an embedding rather than carpals (EM) and one model loaded via the carpals connected with a tie constraint to the cartilage (TM) (Figure 1). The embedding was modelled as a polyurethane (E=1.45GPa and v=0.3) (Synek et al., 2015) cylinder with diameter of 50mm connected to the radius and cartilage using a tie constraint. Load magnitude and BCs were identical to the RM. For the TM, the cartilage was extruded to the proximal surface of the carpals. These two models were referred to as uniaxial loaded models EM_u and TM_u. Furthermore, statically equivalent loads to the RM were applied to both simplified models. Therefore, the necessary forces and moments to be applied at the reference node were calculated based on static equilibrium equations. These two models were referred to as multiaxially loaded models EM_m and TM_m (Figure 1).

2.4. Evaluation of differences

The stress distribution between the intact bone RM and the simplified models were compared elementwise since the models shared the same bone mesh topology. The effective stress $\bar{\sigma}$, defined as $\bar{\sigma}=\sqrt{2EU}$, where E is the Young's modulus and U the strain energy density, was used as an equivalent stress variable. The error was evaluated as the root mean square error, normalized by the mean stress (NRMSE) in different regions. First, the NRMSE was computed in 1mm slices from distal to proximal throughout the entire bone ($NRMSE_{Slice}$). Second, the NRMSE was evaluated for the entire subchondral and Colles' fracture region ($NRMSE_{Region}$). The Colles' fracture region was defined at 22±4mm proximal from the tip of the radial styloid process (Eastell et al., 1989). Cortical and trabecular regions were analyzed separately.

For the fractured bone models with VLP treatment, stresses in the distal fracture fragment were analyzed in analogy to the intact bone model. Three additional parameters were evaluated: 1) FGM, 2) peak von Mises stresses in the plate and 3) distal screw loads at the screw-plate interface. FGM was calculated as the change in distance between two nodes on the dorsal side of the radius on either side of the fracture gap (Figure 1). Peak von Mises stresses in the plate ($\sigma_{vM,peak}$) were evaluated as the 99th percentile to exclude outliers. Screw forces and moments were split into axial force (F_{axial}), shear force (F_{shear}) and the total moment (M_{tot}).

3. Results

3.1. Intact bone models

Qualitative comparison of stress distributions showed that increased complexity of BCs resulted in pronounced stress peaks in the subchondral region (Figure 2). If statically equivalent loads were applied, the error in the embedded model could be reduced considerably, although stress peaks close to the joint were still missing. Quantitative model comparison (Figure 3) revealed that the $NRMSE_{Region}$ was largest for the EM_u in the subchondral trabecular region (133%) and smallest for the TM_m in the cortex of the Colles' fracture region (5%). Furthermore, $NRMSE_{Region}$ was overall larger in the subchondral region compared the Colles' fracture region for all simplified models.

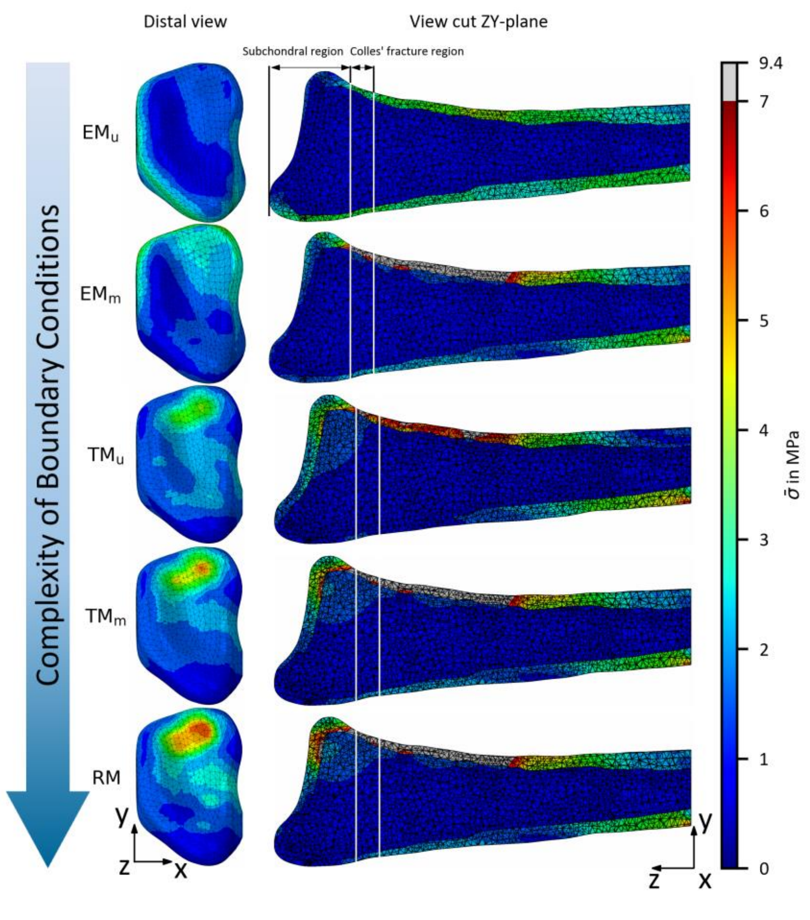

Figure 2: Contour plots of the effective stress ($\bar{\sigma}$) of the intact bone models in ascending order of complexity regarding their boundary conditions. Vertical white lines distinguish the subchondral from the Colles' fracture region.

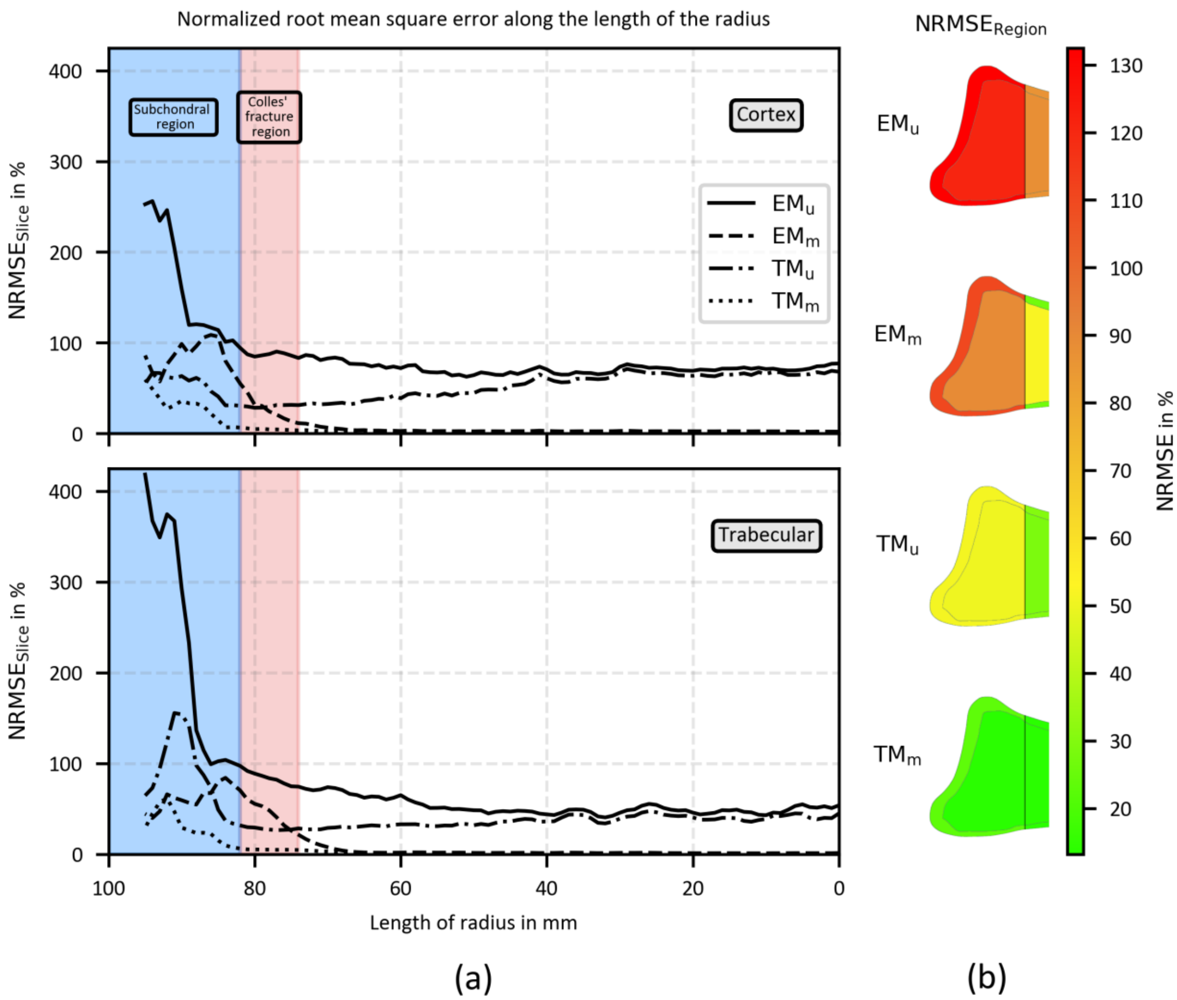

Figure 3: (a) Normalized root mean square error ($NRMSE_{Slice}$) of the effective stress ($\bar{\sigma}$) along the bone between the reference model (RM) and the simplified models (EM_u, EM_m, TM_u and TM_m) for cortex and trabecular region. (b) NRMSE of the subchondral and trabecular regions ($NRMSE_{Region}$) displayed as a colormap representation of the bone sections.

3.2. Fractured bone models

Qualitatively, the fractured bone model with VLP showed less pronounced stress peaks in the subchondral bone for the embedded models (Figure 4). Still, using statically equivalent loading reduced the error of the embedded model considerably. Quantitatively, largest differences were observed for the EM_u and smallest for the TM_m (Figure 5). Differences in the uniaxially loaded models were larger than 50% for FGM and peak plate stress and reached up to 250% for individual screw loads in the EM_u. Using statically equivalent loading (EM_m), relative differences decreased to less than 30% for the screw loads and less than 6% for FGM and peak plate stresses. If carpals were additionally included (TM_m), the error further decreased to below 10% for all parameters.

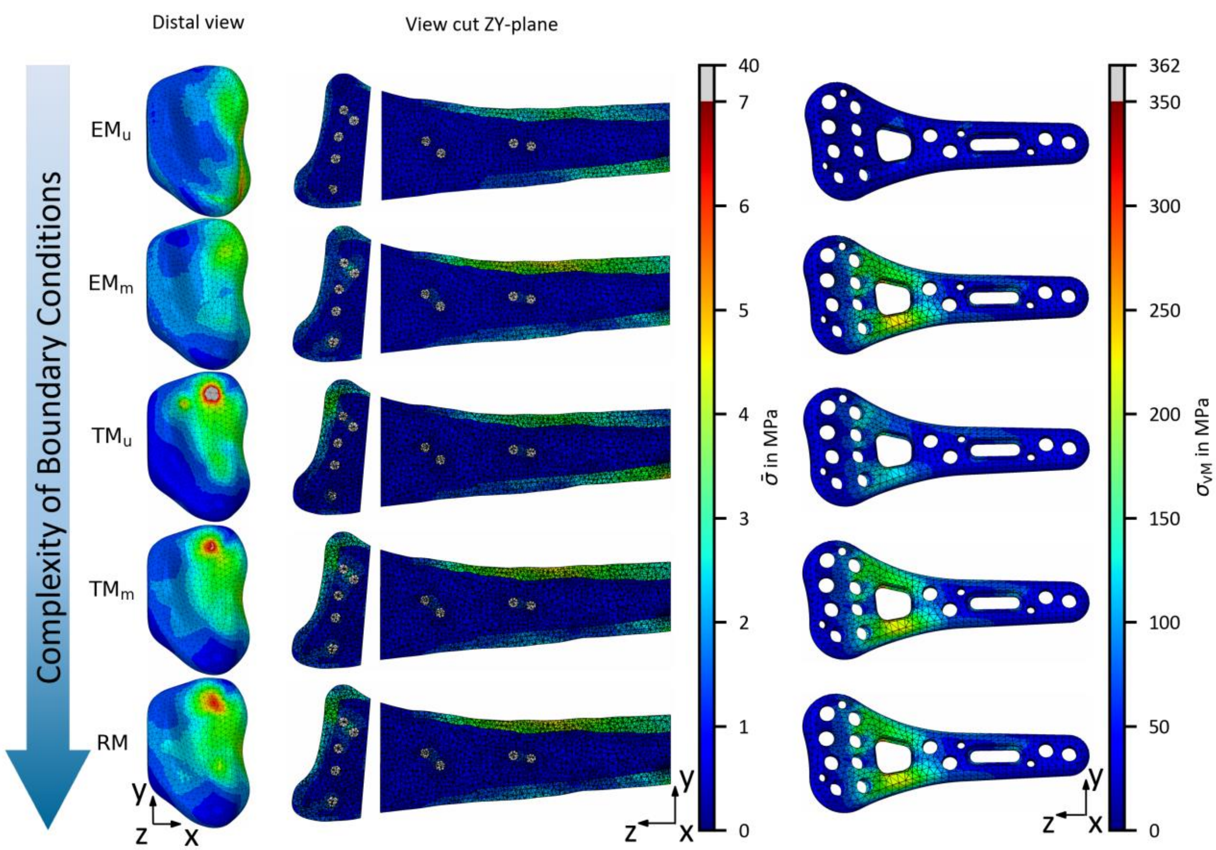

Figure 4: Contour plots of the effective stress ($\bar{\sigma}$) of the bone as well as von Mises stress (σ_{vM}) of the volar locking plate (VLP) of the reference model (RM) and simplified models (EM_u, EM_m, TM_u and TM_m) in ascending order of complexity regarding their boundary conditions.

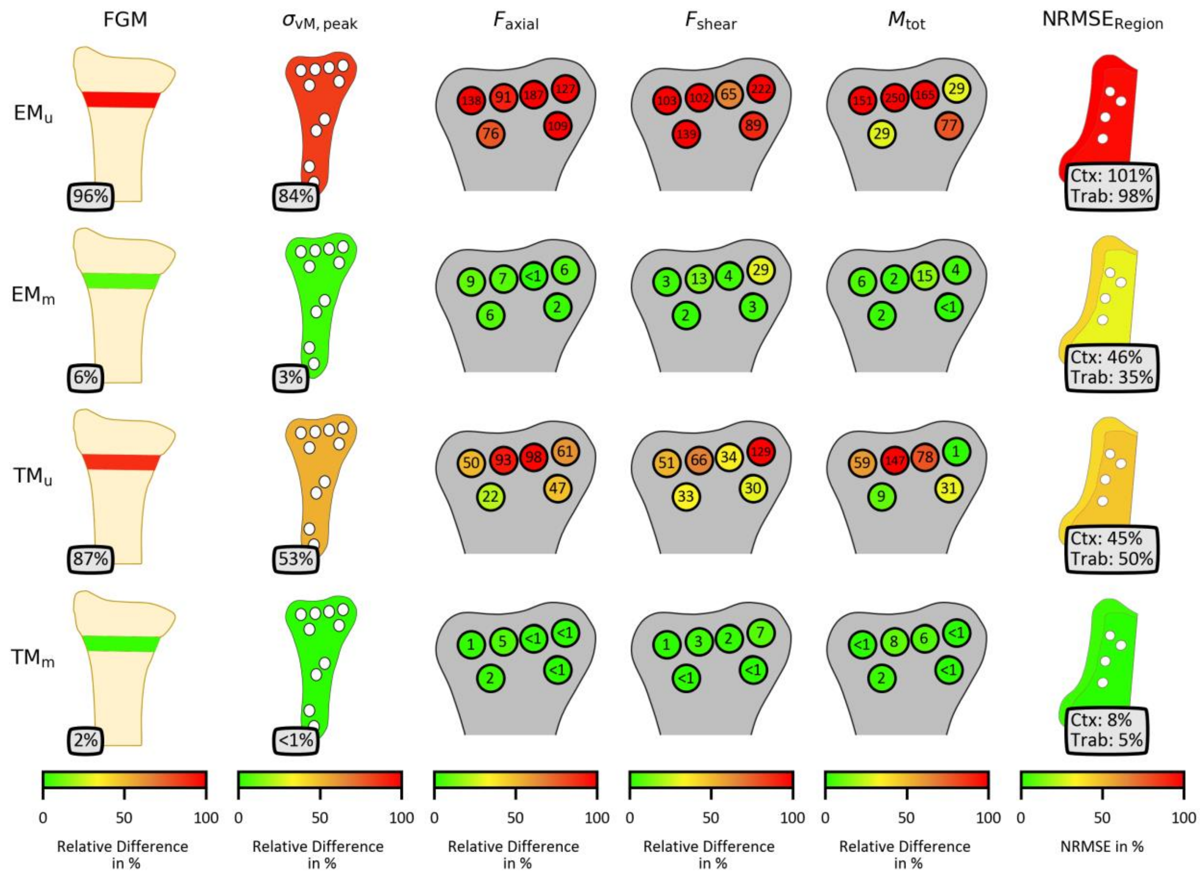

Figure 5: Colormap plots of the relative differences in fracture gap movement (FGM), VLP peak stress ($\sigma_{vM,peak}$), axial screw force (F_{axial}), shear screw force (F_{shear}) and total screw moment (M_{tot}) and regional normalized root mean square error ($NRMSE_{Region}$) of the fracture fragment of the radius. Values of differences are presented for each condition in grey boxes or on top of the respective screws.

4. Discussion

Overall, the results showed that simplified BCs at the RCJ can affect both the stress distribution in the distal radius and the simulation outcomes of the fractured radius with VLP treatment.

In the intact distal radius, stresses in the Colles' fracture region were generally less affected by simplified BCs compared to subchondral bone stresses. However, using uniaxial loading instead of statically equivalent loads in the embedded models still led to considerable errors in the Colles' fracture region. This result is in line with Johnson and Troy (2018), who reported differences of the load distribution in the fracture region between physiological and uniaxial loading at the RCJ. In addition to their study, our results indicate that carpals do not necessarily need to be included for realistic stress distributions in the fracture region if realistic multiaxial loading is applied. This is supported by Varga et al. (2009), who were able to reproduce Colles' fractures in radii using embedding material rather than carpals, but tilted the bone for a more realistic load direction. Additional inclusion of carpals might only be relevant if subchondral bone stresses are investigated. In that case, using tie constraints rather than actual contact led to an acceptable average error (<25%). This also supports the use of simple voxel-based FE models with tied carpals (e.g. Pistoia et al. 2002), rather than creating complex models with smooth surfaces necessary to implement contact interaction.

For the fractured distal radius with VLP treatment, the results were largely consistent with those of the intact bone. Realistic multiaxial loading proved to be of utmost importance for VLP parameters typically assessed in biomechanical studies such as peak implant plate loading and FGM (Caiti et al., 2019). However, caution is warranted if the distribution of loads between screws is investigated, e.g. when comparing screw configurations (e.g. Drobetz et al., 2013), or if peri-implant bone loading is evaluated (e.g. Synek et al., 2021). To provide clinically more realistic results, these models should incorporate load introduction through carpals. As for the intact bone, the contact interaction might be replaced with tie constraints if realistic multiaxial loading is applied, without introducing substantial errors (<10%).

Some limitations of this study must be mentioned. First, no experimental validation was performed. Experimental assessment of stress distributions inside the bone was considered beyond the scope of this paper, as even measuring intraarticular pressure is challenging (Rikli et al., 2007). Second, the BCs in the RMs were still highly simplified. In particular, the carpals were fused, only axial translation was unconstrained, and just one load magnitude was investigated. Still, these loading conditions allowed for systematic comparison of different BCs as well as delineation of effects caused by different resultant loads and local articular stress peaks. Finally, homogenous, isotropic material properties were used for cortical and trabecular bone regions rather than material mapping based on local bone density. This decision was made to include the heterogeneous nature of the distal radius (i.e., thin but stiff cortex and more compliant trabecular bone) despite the low resolution of the available CT scan.

In conclusion, this study suggests that realistic multiaxial loading is most relevant for accurate predictions of the stress distribution in the intact distal radius and mechanical parameters of VLP treatment. Additional inclusion of carpals might only be relevant if subchondral bone stresses, peri-implant bone stresses or individual distal screw loads are investigated. Modelling contact interaction between carpals and radius might be replaced by tie constraints if realistic multiaxial loading is applied.

Conflict of Interest

The authors declare that there are no conflicts of interest.

References

Armstrong, C.G., Lai, W.M., Mow, V.C., 1984. An analysis of the unconfined compression of articular cartilage. J. Biomech. Eng. 106, 165–173. https://doi.org/10.1115/1.3138475

Baumbach, S.F., Schmidt, R., Varga, P., Heinz, T., Vécsei, V., Zysset, P.K., 2011. Where is the distal fracture line location of dorsally displaced distal radius fractures? J. Orthop. Res. 29, 489–494. https://doi.org/10.1002/jor.21268

Baumbach, S.F., Synek, A., Traxler, H., Mutschler, W., Pahr, D., Chevalier, Y., 2015. The influence of distal screw length on the primary stability of volar plate osteosynthesis-a biomechanical study. J. Orthop. Surg. Res. 10. https://doi.org/10.1186/s13018-015-0283-8

Caiti, G., Dobbe, J.G.G., Bervoets, E., Beerens, M., Strackee, S.D., Strijkers, G.J., Streekstra, G.J., 2019. Biomechanical considerations in the design of patient-specific fixation plates for the distal radius. Med. Biol. Eng. Comput. 57, 1099–1107. https://doi.org/10.1007/s11517-018-1945-6

Christen, P., Ito, K., Knippels, I., Müller, R., van Lenthe, G.H., van Rietbergen, B., 2013. Subject-specific bone loading estimation in the human distal radius. J. Biomech. 46, 759–766. https://doi.org/10.1016/j.jbiomech.2012.11.016

Drobetz, H., Weninger, P., Grant, C., Heal, C., Muller, R., Schuetz, M., Pham, M., Steck, R., 2013. More is not necessarily better. A biomechanical study on distal screw numbers in volar locking distal radius plates. Injury 44, 535–539. https://doi.org/https://doi.org/10.1016/j.injury.2012.10.012

Eastell, R., Wahner, H.W., O'Fallon, M., Amadio, P.C., Melton, L.J., Riggs, B.L., 1989. Unequal decrease in bone density of lumbar spine and ultradistal radius in Colles' and vertebral fracture syndromes. J. Clin. Invest. 83, 168–174. https://doi.org/10.1172/JCI113854

Edwards, W.B., Troy, K.L., 2012. Finite element prediction of surface strain and fracture strength at the distal radius. Med. Eng. Phys. 34, 290–298. https://doi.org/10.1016/j.medengphy.2011.07.016

Johnson, J.E., Troy, K.L., 2018. Simplified boundary conditions alter cortical-trabecular load sharing at the distal radius; A multiscale finite element analysis. J. Biomech. 66, 180–185. https://doi.org/10.1016/j.jbiomech.2017.10.036

Kikinis, R., Pieper, S.D., Vosburgh, K.G., 2014. 3D Slicer: A Platform for Subject-Specific Image Analysis, Visualization, and Clinical Support, in: Intraoperative Imaging and Image-Guided Therapy. Springer New York, pp. 277–289. https://doi.org/10.1007/978-1-4614-7657-3_19

Knežević, J., Kodvanj, J., Čukelj, F., Pamuković, F., Pavić, A., 2017. A biomechanical comparison of four fixed-angle dorsal plates in a finite element model of dorsally-unstable radius fracture. Injury 48, 41–46. https://doi.org/https://doi.org/10.1016/S0020-1383(17)30738-6

Liu, H.C., Jiang, J.-S., Lin, C.-L., 2020. Biomechanical investigation of a novel hybrid dorsal double plating for distal radius fractures by integrating topology optimization and finite element analysis. Injury 51, 1271–1280. https://doi.org/https://doi.org/10.1016/j.injury.2020.03.011

Nellans, K.W., Kowalski, E., Chung, K.C., 2012. The Epidemiology of Distal Radius Fractures. Hand Clin. 28, 113–125. https://doi.org/10.1016/j.hcl.2012.02.001

Pistoia, W., van Rietbergen, B., Lochmüller, E.-M., Lill, C.A., Eckstein, F., Rüegsegger, P., 2002. Estimation of distal radius failure load with micro-finite element analysis models based on three-dimensional peripheral quantitative computed tomography images. Bone 30, 842–848. https://doi.org/https://doi.org/10.1016/S8756-3282(02)00736-6

Pollock, J., O'Toole, R. V., Nowicki, S.D., Eglseder, W.A., 2013. Articular cartilage thickness at the distal radius: A cadaveric study. J. Hand Surg. Am. 38, 1477–1481. https://doi.org/10.1016/j.jhsa.2013.04.037

Rikli, D.A., Honigmann, P., Babst, R., Cristalli, A., Morlock, M.M., Mittlmeier, T., 2007. Intra-Articular Pressure Measurement in the Radioulnocarpal Joint Using a Novel Sensor: In Vitro and In Vivo Results. J. Hand Surg. Am. 32, 67–75. https://doi.org/10.1016/j.jhsa.2006.10.007

Saint-Venant, B. de, 1855. Memoire sur la Torsion des Prismes. Mem. Divers Savants 14, 233–560.

Sander, A.L., Leiblein, M., Sommer, K., Marzi, I., Schneidmüller, D., Frank, J., 2020. Epidemiology and treatment of distal radius fractures: current concept based on fracture severity and not on age. Eur. J. Trauma Emerg. Surg. 46, 585–590. https://doi.org/10.1007/s00068-018-1023-7

Schindelar, L.E., Ilyas, A.M., 2021. Plate Fixation of Distal Radius Fractures: What Type of Plate to Use and When? Hand Clin. 37, 259–266. https://doi.org/10.1016/j.hcl.2021.02.008

Swiss Institute for Computer Assisted Surgery, 2020. SMIR - SICAS Medical Image Repository. URL https://www.smir.ch (accessed 3.9.20).

Synek, A., Baumbach, S.F., Pahr, D.H., 2021. Towards optimization of volar plate fixations of distal radius fractures: Using finite element analyses to reduce the number of screws. Clin. Biomech. 82. https://doi.org/10.1016/j.clinbiomech.2021.105272

Synek, A., Borgmann, L., Traxler, H., Huf, W., Euler, E., Chevalier, Y., Baumbach, S.F., 2016. Using self-drilling screws in volar plate osteosynthesis for distal radius fractures: A feasibility study. BMC Musculoskelet. Disord. 17, 120. https://doi.org/10.1186/s12891-016-0972-4

Synek, A., Chevalier, Y., Baumbach, S.F., Pahr, D.H., 2015. The influence of bone density and anisotropy in finite element models of distal radius fracture osteosynthesis: Evaluations and comparison to experiments. J. Biomech. 48, 4116–4123. https://doi.org/10.1016/j.jbiomech.2015.10.012

Varga, P., Baumbach, S., Pahr, D., Zysset, P.K., 2009. Validation of an anatomy specific finite element model of Colles' fracture. J. Biomech. 42, 1726–1731. https://doi.org/10.1016/j.jbiomech.2009.04.017

Wu, G., Van Der Helm, F.C.T., Veeger, H.E.J., Makhsous, M., Van Roy, P., Anglin, C., Nagels, J., Karduna, A.R., McQuade, K., Wang, X., Werner, F.W., Buchholz, B., 2005. ISB recommendation on definitions of joint coordinate systems of various joints for the reporting of human joint motion - Part II: Shoulder, elbow, wrist and hand. J. Biomech. 38, 981–992. https://doi.org/10.1016/j.jbiomech.2004.05.042

Yamazaki, T., Matsuura, Y., Suzuki, T., Ohtori, S., 2021. Evaluation of fixation after plating of distal radius fractures - a validation study. Comput. Methods Biomech. Biomed. Engin. 24, 1687–1692. https://doi.org/10.1080/10255842.2021.1909576